Deformation and failure mechanism of nano-composite coatings under nano-indentation

Galvan, D.; Pei, Y.T.; Hosson, J.Th.M. De

Published in:
Surface & Coatings Technology

DOI:
10.1016/j.surfcoat.2005.10.010

Publication date:
2006

Available online at www.sciencedirect.com
SCIENCE DIRECT
Surface & Coatings Technology 200 (2006) 6718–6726
SURFACE & COATINGS TECHNOLOGY
www.elsevier.com/locate/surfcoat

Deformation and failure mechanism of nano-composite coatings under nano-indentation

D. Galvan, Y.T. Pei, J.Th.M. De Hosson *

Department of Applied Physics, Materials Science Center and the Netherlands Institute for Metals Research, University of Groningen, Nijenborgh 4, 9747 AG Groningen, The Netherlands

Received 27 May 2005; accepted in revised form 5 October 2005
Available online 21 November 2005

Abstract

Two nano-composite coatings based on nc-TiC particles in an a-C:H matrix are deposited via closed-field unbalanced reactive magnetron sputtering. The compositions of the coatings are varied by changing the acetylene gas flow during the depositions. A Cr/Cr–Ti/Ti–TiC graded interlayer is introduced between substrate and coating. Electron probe micro-analyses (EPMA) show that the Ti content of the coatings varies between 31.7 and 11.5 at.%. The coatings exhibit a hardness (H) of 20.0 and 15.7 GPa, and a Young's modulus (E) of 229.4 and 136.6 GPa, respectively, as measured through nano-indentations. Cube corner indentations are performed to probe the fracture toughness of the coatings through the determination of critical indentation loads (L_r) at which radial cracks start to propagate. Transmission electron microscopy (TEM) observations and energy-filtered TEM are employed to characterize the coatings nanostructures. The variation in Ti content is accompanied by a variation in TiC particle size and volumetric fraction, as well as a change in the columnar structure of the coatings. A focus ion beam (FIB) slicing technique is employed to prepare samples from nano-indented locations of coated Silicon and stainless steel (SS) substrates. TEM inspection of the FIB sliced samples determines that the most brittle phase in the coating is the C-enriched columnar boundary, and identifies the location of failure within the interlayer. As a consequence of the different nanostructure, the coatings exhibit different elastic recovery properties and toughness.

Keywords: Nano-composite coating; TiC nano-particles; a-C:H matrix; Magnetron sputtering; TEM

1. Introduction

Nano-composite coatings consisting of nano-crystalline TiC (nc-TiC) particles embedded in an amorphous hydrocarbon (a-C:H) matrix are able to combine high fracture toughness and wear resistance with a low friction coefficient. These combined properties are attractive for applications on driveline components in the automotive industry. The excellent tribological properties of such coating systems have been described in detail in [1,2]. Furthermore, a correlation between the deposition parameters and the coating nano-composite structure has been presented in [3], whereas the structure of the graded interlayer introduced between the coatings and substrates has been investigated in [4].

Modern theories of wear consider that parameters such as H/E (related to the elastic strain to failure) and H^3/E^{*2} (related to the resistance to plastic deformation) are more important than hardness alone in determining the wear resistance of a material. E^* is the effective Young's modulus measured by instrumental nano-indentation and is defined as $E^* = E/(1-\nu^2)$, where ν is the Poisson's ratio of the material. The coating toughness is an important parameter in various tribological applications [5,6]. H/E is significant since a hard material such as a ceramic coating can resist abrasive wear, and a low Young's modulus allows property matching with the metallic substrate, which is generally more compliant than a ceramic. Furthermore, a lower Young's modulus of a coating material is expected to allow the redistribution of the applied load over a larger area, delaying failure of the coating/substrate system. H^3/E^{*2} is connected to the yield strength of the material. An increase of H^3/E^{*2} is expected to lead to an improvement of the elastic recovery of the coating, which clearly is also related to the toughness. A

* Corresponding author. Tel.: +31 50 3634898; fax: +31 50 3634881.
E-mail address: hossonj@phys.rug.nl (J.Th.M. De Hosson).

0257-8972/$ - see front matter © 2005 Elsevier B.V. All rights reserved.
doi:10.1016/j.surfcoat.2005.10.010

thorough investigation of the Ti–B–N and Ti–B–C material systems was performed in [7], confirming that the highest H^3/E^{*2} values are obtained at the smallest grain size and highest fraction of phase boundaries. From this point of view nanocomposite coatings may offer promising opportunities for optimized design of wear-resistant coatings.

Another approach to obtain tougher coatings is the suppression of the formation of columnar boundaries, especially if these contain voids that can act as nucleation points of cracks. The influence of the homologous temperature (T/T_m) of the substrates during deposition and the influence of ion bombardment on the columnar structure of coatings has been thoroughly investigated for example in [8,9]; higher substrate temperatures and higher intensity of ion bombardment result in less voids and columnar features forming within the coatings. Recently, a novel structure zone model (SZM) has been developed that is strictly applicable to the "closed field unbalanced magnetron sputtering" film deposition technique (CFUMS) [10]. Such technique yields very high bombarding ion flux towards the substrates. Therefore it suppresses the formation of voids at grain boundaries even at low substrate temperature, due to the considerable rearrangement of the material structure induced by the intense ion bombardment. Increasing the ion flux or ion energy further hamper the formation of columnar features in the coatings.

Experimental determination of the toughness of thin films is a challenge task due to the limited thickness of the films and common approaches, such as tensile tests, suffer from the inevitable influence of the substrate on the deformation behavior. Another possible approach is based on the measurement of the length of the cracks propagating from the corners of indentations. The length of the cracks can be correlated to the toughness of the material [11]. While this procedure is valid for brittle ceramics and thick films, the investigation of the toughness of thin films that exhibit toughness enhancement effects such as nano-composite TiC/a-C:H may still be erroneous as the indentation depth for crack generation and propagation can even exceed the coating thickness itself. Using a cube-corner indenter favors the generation of cracks at lower applied loads [12], but for tough thin films the loads applied to generate cracks has to be so high that the influence of the substrate material is inevitable. Therefore, electron microscopy observation of the areas below nano-indentations is important to determine the possible influence of the substrate on the generation and propagation of cracks. TEM investigation of the areas below nano-indented impressions can also reveal the plastic deformation behavior of the coating material and the failure mechanism. The preparation of TEM samples from such areas with conventional methods [13] is complex and time consuming. The recent development of a focused ion beam (FIB) slicing technique has provided a powerful tool for this kind of investigations. The general technique and possible applications are described in [14].

The present paper concentrates on the TEM characterization of nano-compostite coatings and the post mortem observation of their structure after nano-indentations. The different crack propagation and deformation behavior the coatings exhibit as a consequence of their different nano-structures is investigated. The focused ion beam (FIB) slicing technique is employed to obtain TEM samples from nano-indented locations of coatings deposited on Si and stainless steel (SS) substrates. Based on the experimental results, a method is proposed to qualitatively evaluate the toughness of thin films, through the determination of a critical indentation load, L_r, at which radial cracks *start* propagating from the corners of cube-corner indentations. Furthermore, the proposition that a lower Young's modulus of coating materials permits the redistribution of applied load over larger volumes is verified experimentally.

2. Experimental

Nano-composite nc-TiC/a-C:H coatings were deposited via closed-field unbalanced reactive magnetron sputtering in an argon/acetylene (Ar/C_2H_2) atmosphere with a Hauzer HTC-1000 coating system, which was equipped with two Cr targets and two Ti targets opposing each other and Ar and acetylene gas sources. The detailed set-up of the coating system has been documented elsewhere [15]. The substrates used for each deposition were ø30 × 5 mm discs of hardened M2 steel, 304 SS and ø100 mm Si wafers. A Cr/Cr–Ti/TiC graded interlayer was introduced between substrate and coating to improve adhesion. For details of deposition parameters and structure of the graded interlayer, reference is made to [4]. Two coatings of different Ti content were deposited under an applied substrate bias of −100 V. The Ti content was varied by varying the acetylene gas flow during deposition, 80 sccm C_2H_2 flow for coating 100V80 and 110 sccm C_2H_2 flow for coating 100V110. The depositions were carried out while keeping a constant power applied to the Ti targets, and a constant deposition pressure at 0.33 Pa. No intentional substrate heating was applied during the depositions. Nevertheless, the substrate temperature was monitored with a thermocouple and as a consequence of the ion bombardment the substrates reached temperatures in the 180–190 °C range. The deposition was carried on until a coating thickness of about 1.4 μm was reached.

Electron probe micro-analysis (EPMA) with a Cameca SX-50 wavelength-dispersive (WD) X-ray spectrometer was used to determine the chemical composition of the coatings with the use of standards. An acceleration voltage of 5 keV was employed to avoid excitation of X-rays from the interlayer area of the coating. A fully calibrated MTS Nano Indenter XP was employed to measure the hardness and Young's modulus of the coatings with a Berkovich indenter, using the continuous stiffness measurement technique (CSM), and the fracture toughness with a cube-corner indenter. Nano-indentations were performed at a constant strain rate of 0.02 s^{-1} by controlling the final maximum load or maximum displacement. As the desired load or displacement was reached the nano-indenter tip was held in position permitting creep effects to occur, and during the unloading part of the experiment a correction of thermal drifts was performed. A radial critical load (L_r) was defined as the indentation load at which radial cracks started propagating at the corners of a cube-corner indentation performed on a coated Si substrate. A CSM Revetest scratch tester was used for

measuring the interfacial adhesion strength with a diamond stylus of 200 μm radius and 0.01 m/min scratch speed.

A Philips XL30S FEG scanning electron microscope (SEM) was employed to study the fractured cross-sectional structure of the samples and the crack propagation after nano-indentation. Low acceleration voltage (3 kV) and small working distance (3 mm) were employed to improve the obtained resolution, and the special through lens detector (TLD) of the microscope was used in high resolution mode (HR-SEM). The investigation of the nanostructures was carried out with a high-resolution TEM (HR-TEM) (JEOL 4000 EX/II, operated at 400 kV) and an analytical TEM (JEOL 2010F-FEG, operated at 200 kV). Bright field (BF), high-resolution (HR), selected area electron diffraction (SAED) and energy filtering (EF) imaging techniques were employed to characterize planar and cross-sectional samples of the coatings. A Gatan image filtering (GIF) system was employed to acquire energy-filtered (EF) images with the three-window technique. The energy window width was set at 20 eV and the frame acquisition time at 30 s. Background-subtracted intensity maps were acquired of the CK, TiL_{32} and CrL_{32} electron energy loss edges over an area of 410×410 nm. The planar samples for electron microscopy were prepared by cutting, grinding, dimpling and ion milling to electron transparency coated stainless-steel substrates. The method described in [16] was used to prepare cross-sectional samples. Focused ion beam (FIB) was employed to cut samples along cracks developing in the coatings at the corners of cube-corner indentations performed on coated Si substrates, and corresponding to the nano-indenter tip for nano-indentations performed on stainless steel substrates. The details of the procedure followed to prepare the FIB samples are further described in [17].

3. Results

3.1. Microstructure of TiC/a-C:H nanocomposite coatings

The results of the compositional analysis and the measured mechanical properties are reported in Table 1. An increase of both the H/E and H^3/E^{*2} parameters is observed at lower Ti content in coating 100V110. From the compositional analysis, the volume fraction V_F of TiC nano-particles within the coatings was estimated through the procedure further explained in [3], yielding a V_F value of 0.6 in coating 100V80 and 0.3 in coating 100V110, respectively.

Table 1
Coating deposition parameters and corresponding properties

Coating properties summary		
Coating name	100V80	100V110
Acetylene gas flow [sccm]	80	110
Ti content [at.%], from EPMA	31.7	17.8
TiC, V_F	0.6	0.3
Hardness [GPa]	20.0	15.6
Effective Young's modulus, E^* [GPa]	237.1	141.2
H/E	0.087	0.114
H^3/E^{*2} [GPa]	0.14	0.19
Lc1 [N]	32	38
L_r (mN)	56.8	86.4

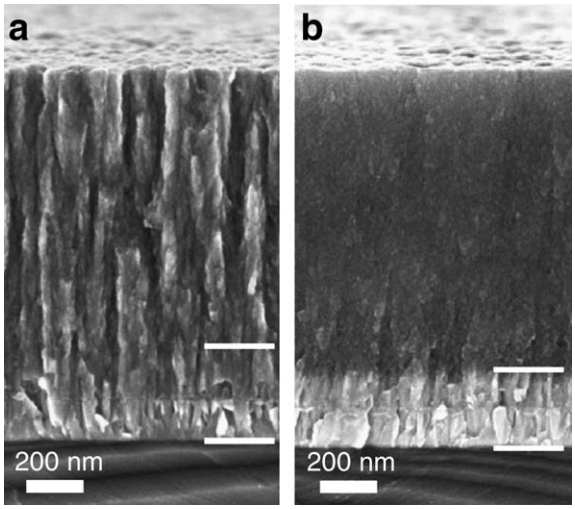

Fig. 1. SEM cross-sectional micrographs of coating 100V80 (a) and 100V110 (b). The Si substrate (bottom), the interlayer (middle) and the coating (top) are visible (delimited by white marks). The structure of the coatings changes from columnar (100V80) to glassy-like (100V110) as the Ti content decreases from 31.7 at.% to 17.8 at.%.

SEM micrographs of the cross-sections of the coatings are displayed in Fig. 1. The coatings nucleate and grow over the interlayer up to a thickness of about 1.4 μm. The change in Ti content brings about a considerable change in the columnar structure of the coatings, and is further inspected below.

Cross-sectional TEM micrographs of coatings 100V80 and 100V110 are reported in Fig. 2. Diffraction rings corresponding

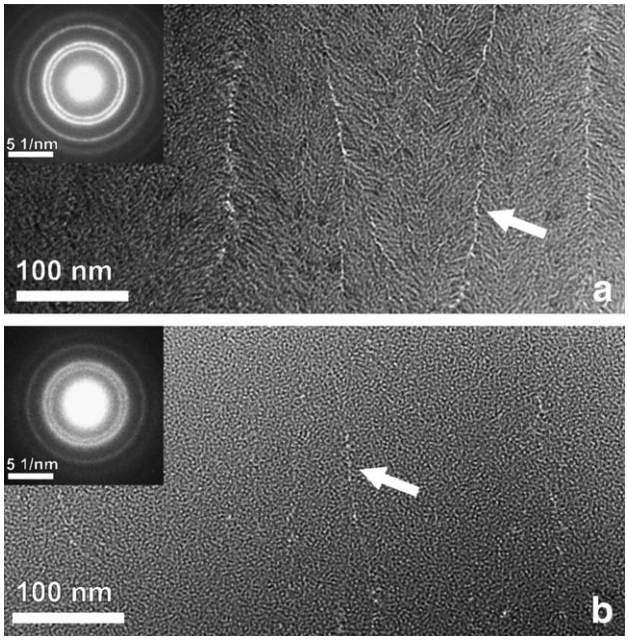

Fig. 2. Cross-sectional TEM micrographs of coatings 100V80 (a) and 100V110 (b). The substrate is located at the bottom of each picture, the coating surface at the top. DP insets are included. The column interfaces (indicated by arrows) are continuous and branched in coating 100V80, thin and discontinuous in coating 100V110.

to the TiC B1 phase were recorded for each sample (see insets in Fig. 2). The intensity of the DP rings varies between the two samples, as compared with the intensity of the transmitted central beam. No preferential orientations for the TiC phase were observed. In both coatings, columns develop of widths around 100 nm perpendicularly to the substrate plane. The columns run through the whole coating thickness and are separated by columnar boundaries (indicated by arrows in Fig. 2). The columnar boundaries of coating 100V80 are clearly visible and their thickness is around 8–10 nm. Each column shows a tree-like structure of brighter ramifications. The columnar boundaries are formed in the location where the ramifications of two neighboring columns meet. The columnar boundaries in coating 100V110 appear thinner and discontinuous as compared with the ones observed in coating 100V80. The thickness is around 5–7 nm, but its growth is often interrupted with a spacing of 10–50 nm. Moreover, no tree-like features are observed within the columns. EF-TEM investigation of the columnar boundaries determined that they are carbon-enriched as compared to the column bodies [4]. Contrast due to the presence of nanoparticles is visible within the columns in coating 100V80, whereas in coating 100V110 the columns appear rather featureless. HR-TEM has been employed to study plan-view samples of the coatings, since the technique used to prepare the plan-view samples yields thinner specimens that allow clear observation of individual TiC nano-particles. On the HR-TEM micrographs shown in Fig. 3, the TiC particle size clearly differs between the two coatings; a thorough investigation of the particle size and size distribution [3] determined that the average TiC particle size is 4.5 nm and 2.2 nm in coatings 100V80 and 100V110, respectively.

3.2. TEM study of deformation and failure modes

3.2.1. Coatings on Si

It was noticed that the crack propagation pattern varied between the two coatings under nano-indentation. Cracks propagating from the corners of cube-corner indentations are depicted in Fig. 4. The indentations were performed on coated Si (100) substrates with the nano-indenter in the load control mode, up to a maximum load of 190 mN. Fig. 4 shows that the radial cracks propagate along the column boundaries or straight through the columns in coatings 100V80 and 100V110,

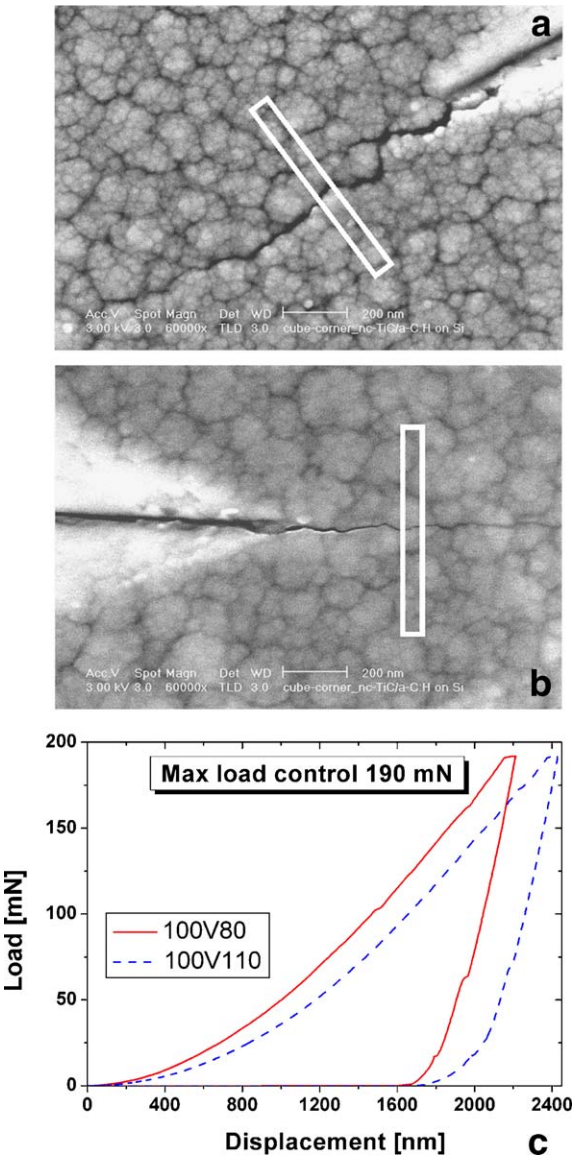

Fig. 4. SEM image of cracks propagating from the edge of cube-corner indentations. White boxes indicate where FIB samples were obtained for coating 100V80 (a) and 100V110 (b), respectively. The relative indentation load–displacement curves are displayed (c), the final indentation depth exceeds the coating thickness.

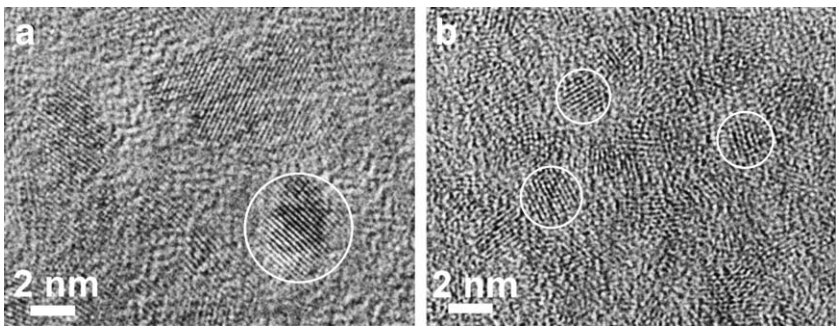

Fig. 3. Planar HR-TEM image of coating 100V80 (a) and 100V110 (b). The TiC particle size clearly increases with increasing Ti content (31.7 at.% in 100V80 and 17.8 at.% in 100V110).

respectively. TEM specimens were prepared by FIB slicing at the sites indicated by white boxes for both coatings. The corresponding indentation load–displacement curves are also shown in Fig. 4c. Due to the high load applied the final indentation depths exceed the coating thickness (1.4 μm). It was observed in previous studies [18] that pop-up events occur as the nano-indenter is retracted from the material in analogous experiments. The pop-up events are related to crack propagation, and they result in the formation of annular cracks around the indentation. These cracks were not observed in the present experiments. In Fig. 5 both specimens are shown as observed in SEM. It is clear that the failure initiates within the underlying Si substrates, which hinders any precise quantification of the fracture toughness value through the measurement of the crack length, a procedure valid for brittle materials and thicker films [11]. For this reason, a different approach was employed in the present case to evaluate the load thresholds for crack propagation, which is qualitatively related to the fracture toughness of the coatings. The approach adopted is similar to the determination of Weibull statistical distribution functions [19] for the survival probability of materials subjected to different loads. Our method relies on the observation of the *number* of cracks propagating within the coating after indentation, instead of measuring their *length*. For this reason the experiments are performed at lower loads, reducing the influence of the substrate material. Counting the cracks is a quicker procedure as compared to measuring their length. Sets of 5 nano-indentations were performed at different loads, up to material failure. Subsequently the samples were observed in the HR-SEM, to determine the average number of cracked corners for each load. Curves were drawn of the percentage of cracked corners as a function of the load applied to the cube-corner indenter, as shown in Fig. 6. Because of their characteristic S shape these curves were fitted with a sigmoidal function, setting the upper and lower boundaries at 0 and 100%, respectively. The inflection point of the curves is then located around the 50% value for the ordinate axes, and this is a convenient location of the curves where a threshold load for crack propagation can be set. Therefore, the critical indentation load (L_r) is defined as the load at which statistically half of the corners have undergone cracking. Since the observed cracks initiate in the Si-wafer and propagate upwards, no relation between the flaws size distribution in the material and the

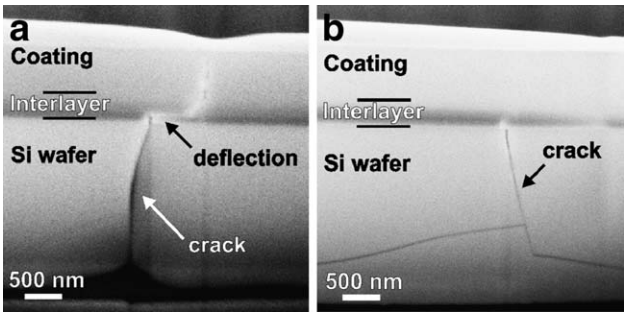

Fig. 5. SEM micrographs of the FIB samples obtained from the locations indicated in Fig. 4, for coating100V80 (a) and 100V110 (b). Arrows indicate the running crack and the location of crack deflection within the interlayer.

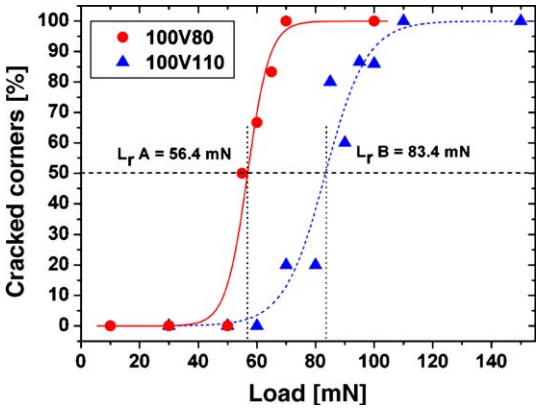

Fig. 6. Sigmoidal curves of the percentage of cracked corners as a function of the indentation applied load for coatings 100V80 and 100V110.

critical load exists, but instead this ranks the different tendency to crack *propagation* of the different materials rather than crack nucleation. Attention should be paid to the orientation of the nano-indenter ridges relative to the cleavage directions of a coated Si-wafer, so that no preferential crack propagation is observed along one of the corners of the nano-indenter impression. Furthermore, both the interlayer and the coating thickness will influence the initiation of cracks observed on the coating surface, and should be kept constant for a reliable comparison of results from different coatings. In the present experiment the Si wafers cleavage plane was misaligned with respect to the nano-indenter ridges, and the coatings interlayer and thickness were constant. Therefore the determination of L_r can give a qualitative indication of the relative toughness of the different coatings. L_r varies between 56.8 and 83.4 mN for coatings 100V80 and 100V110, respectively, to indicate that smaller particle size and thinner column boundaries result in tougher coatings. Although the L_r values determined in such a way are not connected to the value of fracture toughness, it

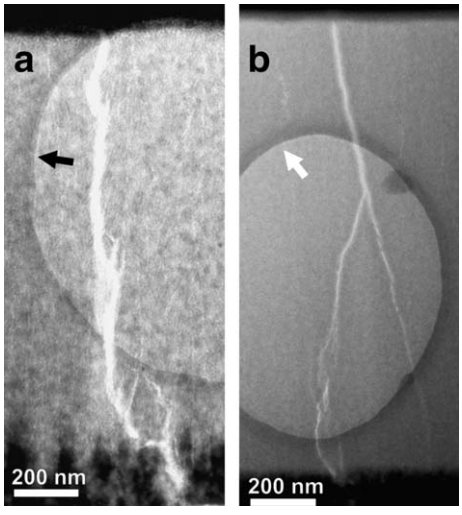

Fig. 7. TEM micrographs of FIB sliced samples from the locations indicated in Fig. 4 for coatings 100V80 (a) and 100V110 (b), respectively. The cracks propagate through a column boundary in coating 100V80 and along the column body in coating 100V110. The circles indicated by arrows in the center of the micrographs are due to the presence of a sample-supporting holey carbon grid.

provides a simple and quick procedure to rank different coatings in terms of their resistance to crack propagation. The TEM investigation in Fig. 7 shows that each crack nucleates in the Si substrate; subsequently it propagates through the interlayer and finally through the coating up to its surface. The propagation of the crack follows a column boundary in coating 100V80, as the crack branching clearly relates to the columnar boundary ramifications shown in Fig. 2, and the final crack direction is exactly perpendicular to the substrate plane, so as to follow the column boundaries. The crack seems to follow a random path in coating 100V110, therefore in this case the column boundaries, which are discontinuous and roughly perpendicular to the substrate surface, do not influence the crack path.

It is clear from Fig. 5 that the crack propagating from the Si substrate side is deflected at a certain location within the interlayer, indicated by an arrow in Fig. 5a. This is observed in both coatings 100V80 and 100V110, even though it is not clearly visible for coating 100V110 in Fig. 5b. The interlayer consists of the consequent stacking of crystalline Cr, Cr rich β-(Cr, Ti) phase, amorphous Cr–Ti phase with β-phase nano-crystals dispersed within it, α-Ti, TiC layers [4]. In Fig. 8 the area of fracture is depicted together with the elemental maps of C, Ti and Cr. It is clear from the elemental maps that the failure occurs as soon as the Cr flux to the substrate is interrupted. This is confirmed both by the elemental maps and the HR-TEM image in Fig. 9. Analyses described in [4] determined that the presence of Cr is connected with the formation of an amorphous/nanocrystalline Cr–Ti phase, on top of which a gradual transition from Ti to TiC crystalline columns occurs as the Cr content drops to zero and the C content is gradually increased. Although the HR-TEM image shows that few tiny crystalline remnants can be found on the bottom side of the crack as indicated by an arrow in Fig. 9b, it is distinct that the crack propagates along the interface between the amorphous Cr–Ti and α-Ti sub-layers. The granular contrast observed within the indicated crack area is due to the presence of the amorphous sample-supporting holey-carbon grid, and is not related to the amorphous Cr–Ti phase.

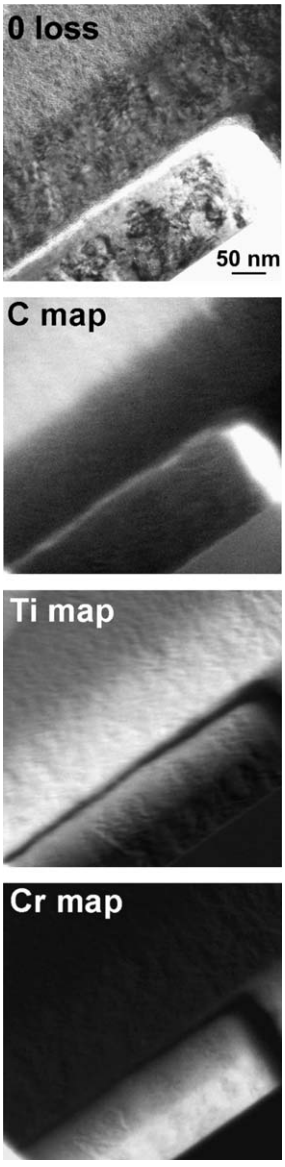

Fig. 8. (From top to bottom) BF image of the area of crack propagation within the interlayer (see text), C map, Ti map, Cr map.

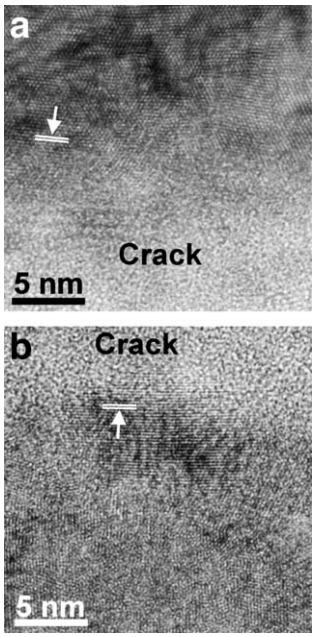

Fig. 9. HR-TEM images above (a) and below (b) the running crack in Fig. 8. Arrows indicate the presence of a crystalline phase on both sides of the crack.

3.2.2. Coatings on stainless steel

Another TEM study has been performed for both coatings deposited on SS substrates after nano-indentation. The low yield stress of SS substrates generally results in plastic flow under large indentation depths. At the onset of plastic flow in the substrate the load is transferred through the coating to the substrate that deforms accordingly. Since the coating is generally not able to accommodate the resulting deformation of the underlying substrate, tensile stresses develop parallel to the substrate surface within the coating, and cracking of the layer can occur [17]. The indentations were performed on both coatings 100V80 and 100V110 with a cube corner indenter up

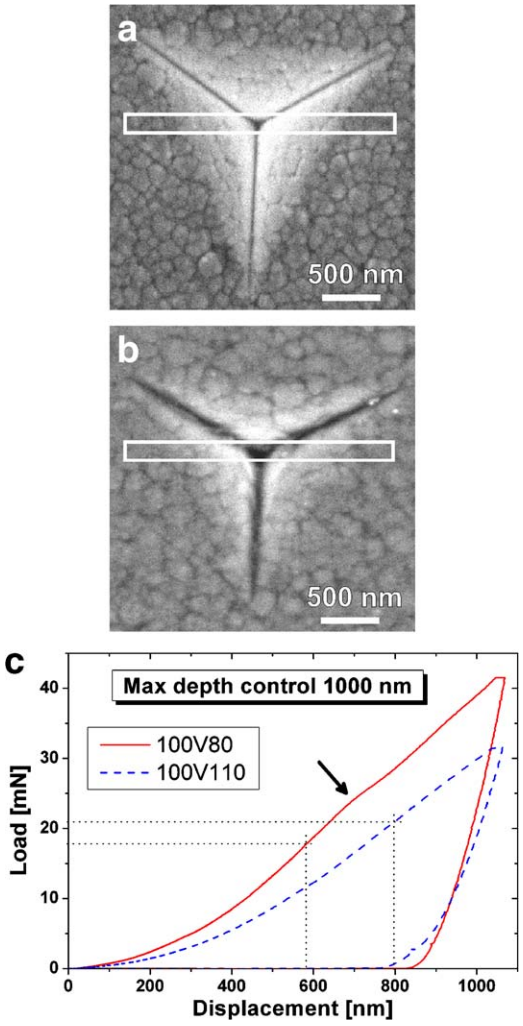

Fig. 10. Indentation marks for coating 100V80 (a), coating 100V110 (b), and the relative load–displacement curves (c). White boxes in (a) and (b) indicate the locations where FIB samples were obtained, and hashed lines in (c) indicate the loads and displacements at which plastic yielding of the SS substrate occurs for coatings 100V80 and 100V110, respectively. An arrow indicates the load at which further cracking occurs in sample 100V80 (see text).

to a fixed indentation depth of 1000 nm. The SEM micrographs of the indented locations are reported in Fig. 10a–b. A shallower indentation impression is observed for coating 100V110. The relative load–displacement curves are reported in Fig. 10c. As the indenter penetrates the material, the contact area increases progressively following a power law behavior characteristic of the indenter employed (indenter area function), so that the rate of increase of contact area exceeds the one of indentation depth. For this reason when the indenter penetrates a homogeneous material the loading part of the load–displacement curve has a positive curvature that increases progressively with indentation depth, in accordance with the power law for the contact area. The analysis of the derivative of the load displacement curves in Fig. 10c indicated that at certain indentation depths (indicated by hashed lines in Fig. 10c) the curvature of the load–displacement curve starts to decrease, instead of increasing gradually as expected for a homogeneous material. Since the coatings are homogeneous throughout their thickness, these points can be identified as the points where plastic flow starts within the SS substrate, which is considerably softer than the coating. The plastic flow in the SS substrate occurs in sample 100V80 at a load of 17.4 mN, or at the indentation depth of 577 nm. Besides this load–displacement curvature change a further inflection of the curvature occurs for a higher load and is indicated by an arrow in Fig. 10c. This is connected with the generation of cracks within the coatings and will be discussed later. In sample 100V110 a negative change of curvature can be identified at 21.0 mN load or at the indentation depth of 799.8 nm. The higher indentation load necessary to reach the preset indentation depth for coating 100V80 is clearly connected to the fact that coating 100V80 is harder than coating 100V110 (20.0 and 15.6 GPa vs. 41.5 and 31.4 mN load). The TEM inspection of the FIB sliced samples is reported in Fig. 11, where the coatings are observed in cross-section. In sample 100V80 the substrate and interlayer below the coating clearly failed, i.e. a crack is present directly below the nano-indenter tip and additional cracks are observed on the sides of the indentation, propagating perpendicular to the substrate surface. In coating 100V110 only a modest plastic deformation of the substrate is observed. Only one crack is present directly below the nano-indentation apex, where the tensile stresses are the highest. Since the substrate deforms plastically below the coating it is not possible to compute elastic recovery values (the ratio of elastic to total deformation), nevertheless by observing both the indentation impressions in Fig. 10 and the TEM

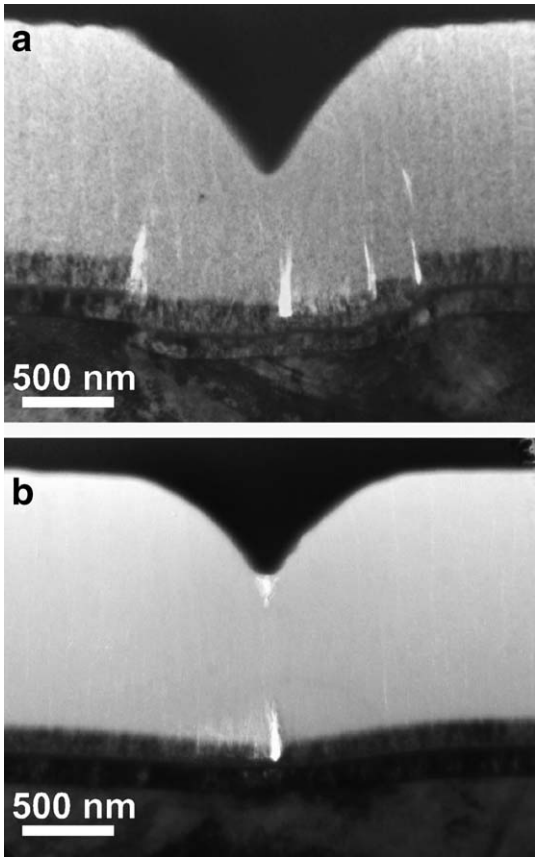

Fig. 11. TEM micrographs from FIB samples prepared from nanoindentations of sample 100V80 (a) and 100V110 (b). Less cracking is observed for coating 100V110, together with a better elastic recovery.

indentation cross-section in Fig. 11 it is clear that coating 100V110 exhibits better elastic recovery than coating 100V80, as the indentation walls are curved manifesting a higher degree of elastic recovery. The adhesive critical loads Lc1 of the coatings deposited on hardened M2 steel were identified at 32 and 38 N for coatings 100V80 and 100V110, respectively.

4. Discussion

The different TiC content in coatings 100V80 and 100V110 influences the intensity of the DP rings shown in Fig. 2. The intensity of the rings probably also correlates with the different particle size measured, as larger particles are able to produce more intense and narrower diffraction reflections. The variation of Ti content influences the width and continuity of the column boundaries, as clearly shown in Fig. 2. The column boundaries are growth defects, and they have already been reported for analogous coatings [20]. In our case it was determined that they consist of C-enriched areas, which do not contain voids, as the C concentration variation has been clearly identified through EF imaging in [4]. Due to the high bombarding ion flux characteristic of the CFUMS technique no voids form, nevertheless columnar features are present as growth defects. These defects are due to shadowing effects occurring when the spherical growth fronts of the columns shadow underlying portions of the coating. The a-C:H matrix is able to incorporate moderate fractions of Ti atoms (<2.5 at.% as determined in [21]) prior to the nucleation and growth of TiC crystals. No crystalline phases were observed within these columnar boundaries. Therefore it is concluded that they incorporate between 0 and 2.5 at.% of Ti, and their structure is the one of fully amorphous (Ti-doped) a-C.

The indentations displayed in Fig. 4 and the TEM investigation in Fig. 7 indicate that the cracks follow the C-enriched column boundaries when these are thick and continuous, as in coating 100V80, and propagate straight through the column bodies (the nanocomposite) when the columnar feature is weaker, as in coating 100V110. This observation points to the superior toughness of the nanocomposite with respect to (doped) a-C. Nevertheless, it must be considered that the mechanical properties of the (doped) a-C and the TiC-containing nano-composite differ from each other. This implies that the two materials will experience different stresses when they deform together. Furthermore, shear stresses are likely to be generated as a consequence of the applied load. The difference in mechanical properties can favor the initiation of cracks at these locations. This effect is stronger the larger the difference in mechanical properties of the two materials. The mechanical properties of a-C:H depend on the hydrogen content and the sp^3/sp^2 hybridization ratio of the carbon network, which in turn depend strongly on the deposition parameters and the material precursors employed. A detailed list of references about this topic is included in our recent paper [22]. The great range of mechanical properties achievable with C-based coatings would permit to match the properties of the nanocomposite columns and the amorphous columnar boundaries from the mechanical point of view (i.e. same elastic modulus and hardness). This approach could possibly increase the toughness of the columnar boundaries within the coating. Nevertheless, toughening effects seem to derive from the dispersion of TiC nano-particles in a-C, suggesting that the total lack of columnar boundaries would lead to a further toughness enhancement.

In the study performed on the coated Si substrates and reported in Figs. 4–7 the indentation depth exceeds the coating thickness, for this reason cracks nucleate within the Si substrate while it is penetrated by the nano-indenter tip. Subsequently the cracks propagate through the coating, but since they are not generated within the coating the fracture toughness cannot be accurately evaluated with the Lawn-Evans-Marshall approach [11]. Here we propose to determine the critical indentation load L_r for radial crack propagation by a simple method that allows ranking of the mechanical performance in terms of their resistance to crack propagation when the same coating thickness and interlayer material are employed. The higher L_r value of coating 100V110 is due to the lower concentration, continuity and thickness of its columnar boundaries as compared to the ones of coating 100V80. Furthermore, the lower TiC V_F and the finer microstructure of coating 100V110 result in enhanced H^3/E^{*2} parameter. This result agrees with observations reported by other authors relating a finer nano-structure with an improved resistance to plastic deformation H^3/E^{*2} [7].

The study performed on the SS substrates is interesting as it determined that in coating 100V110, of lower elastic modulus, the plastic deformation within the underlying SS substrate occurs at a higher load as compared to coating 100V80. This is an experimental confirmation of the concept in the design of tribological coatings that a coating of low elastic modulus is desirable since it permits the redistribution of the locally applied load over a larger volume, delaying the onset of plastic deformation in the substrate and subsequent cracking and chipping of the coating. Indeed, the onset of plastic deformation in the substrate is accompanied by the development of tensile stresses on the coating side, close to the substrate-coating interface, which result in the generation of cracks. As the deformation of the substrate progresses shear stresses develop at the interface of the different columns in the coating. These shear stresses result in the nucleation and propagation of additional cracks on the nano-indentations side for coating 100V80, as here the columnar boundaries are thicker and there is significant substrate deformation, whereas in coating 100V110 no such cracks develop as the columnar boundaries are weaker and the substrate deformation is lower. The generation of these additional cracks is clearly visible in the load–displacement curve of coating 100V80 (indicated by an arrow in Fig. 10c). Indeed, the cracks viewed in cross-section in Fig. 11a are expected to propagate and form semi-circles on each face of the cube-corner indenter. While these cracks are not linked to each other or to the median crack, their presence indicates that extensive cracking of the material occurred, to the point that this is visible on the load–displacement curve. Other investigations [17] determined from analogous experiments performed on multilayered coatings that the cracks in that case propagate both perpendicular to the substrate interface and also parallel to it,

corresponding to the periodic variation of mechanical properties caused by the multilayered structure of these coatings, which causes the concentration of shear stresses where cracks can nucleate. Running cracks parallel to the coating surface can easily lead to chipping, the sudden removal of large flakes of the coating material, which leads to higher wear rates and the formation of large abrasive debris in the tribological contact. Since the coatings presently investigated are nano-composite structures that have homogeneous properties along their thickness, no cracks parallel to the substrate surface were observed to propagate as a result of the above-mentioned tensile stress. Instead, the stress is relaxed by the generation of perpendicular cracks. This is indeed a more favorable situation from the point of view of the tribological performance of coatings. Nevertheless, it should be considered that different stress fields exist between the indentation of a faceted stylus and the loading contact of a ball-on-flat wear test or other possible geometries in actual tribological applications.

Besides the change in fracture toughness, the change in TiC particle size, V_F and columnar structure between coating 100V80 and 100V110 brings about a considerable improvement in the coating tribological properties, as was reported in [1]. Furthermore, the decrease in Young's modulus from coating 100V80 to 100V110 is beneficial for the coating adhesion, as the adhesive critical load increases from coating 100V80 to 100V110. Also in this case, a lower Young's modulus permits to redistribute the applied load over a larger area, increasing the load bearing capability of the coating. The graded interlayer always fails where the Cr content drops to zero. HR-TEM investigation determines that the weak portion of the interlayer is the interface between the amorphous Cr–Ti and α-Ti sub-layers, indicating that in that location a functional discontinuity of the graded structure exists. It suggests that the presently employed graded interlayer scheme is not optimal as the gradual change in composition is not accompanied by an equally gradual change in mechanical properties.

5. Conclusions

The deformation of nano-composite coatings was studied at high indentation loads (Si substrates) and at low indentation loads (SS substrates), respectively. In the former case crack propagation behavior was observed, pointing to the conclusion that no classical approach is valid to measure the fracture toughness of a tough thin film/coating, since the cracks originate from the underlying Si substrate. An alternative approach is proposed that relies on the determination of the critical indentation load L_r at which radial cracks start to propagate. C-enriched columnar boundaries should be avoided, especially when they continuously extend through the whole coating thickness. TEM observations determined that the change in Ti content influences the TiC particle size and the columnar structure of the coatings. A lower concentration of Ti may limit the formation of interfacial a-C between the columns, increasing the overall coating toughness. Furthermore, lower TiC V_F and smaller particle size result in an increase of the H/E and H^3/E^{*2} parameters. A high H^3/E^{*2} leads to an improved elastic recovery of the coating after indentation. Furthermore, the study gives experimental evidence that a lower Young's modulus of the coating material permits the redistribution of an applied load over a larger area, delaying the onset of plastic yielding of the underlying substrate and the subsequent failure within the coating due to tensile stresses developing close to the coating–substrate interface. As compared to multi-layered hard coatings, in the nano-composite coatings investigated no cracks develop parallel to the coating surface after deformation, which can be an advantage when resistance to chipping and delamination should be met in tribological coatings.

Acknowledgements

Albano Cavaleiro of the University of Coimbra, Portugal is gratefully acknowledged for the EPMA measurements, Valerie Sivel from TU Delft (NL) for the preparation of the FIB samples, Christian Strondl from Hauzer Technocoating BV (Venlo, NL) for his help in the deposition of the coatings. The authors acknowledge financial support from the Netherlands Institute for Metals Research (NIMR) and the Foundation for Fundamental Research on Matter (FOM-Utrecht).

References

[1] Y.T. Pei, D. Galvan, J.Th.M. De Hosson, Acta Mater. 53 (17) (2005) 4505.
[2] J.Th.M. De Hosson, Y.T. Pei, D. Galvan, A. Cavaleiro, Mater. Res. Soc. Symp. Proc. 843 (2005) T1.6.1.
[3] D. Galvan, Y.T. Pei, J.Th.M. De Hosson, Surf. Coat. Technol. (submitted for publication).
[4] D. Galvan, Y.T. Pei, J.Th.M. DeHosson, Acta Mater. 53 (14) (2005) 3925.
[5] A. Leyland, A. Matthews, Wear 246 (2000) 1.
[6] A. Leyland, A. Matthews, Surf. Coat. Technol. 177–178 (2004) 317.
[7] P.H. Mayrhofer, C. Mitterer, J. Musil, Surf. Coat. Technol. 174–175 (2003) 725.
[8] J.A. Thornton, J. Vac. Sci. Technol., A 4 (6) (1986) 3059.
[9] J.A. Thornton, J. Vac. Sci. Technol. 11 (1974) 666.
[10] P.J. Kelly, R.D. Arnell, J. Vac. Sci. Technol., A 16 (5) (1998) 2858.
[11] B.R. Lawn, A.G. Evans, D.B. Marshall, J. Am. Ceram. Soc. 63 (1980) 574.
[12] G.M. Pharr, Mater. Sci. Eng., A 253 (1998) 151.
[13] N.J.M. Carvalho, J.Th.M. De Hosson, J. Mater. Res. 16 (2001) 2213.
[14] J.M. Cairney, P.R. Munroe, M. Hoffman, Surf. Coat. Technol. (in press).
[15] C. Strondl, N.M. Carvalho, J.Th.M. De Hosson, G.J. van der Kolk, Surf. Coat. Technol. 162 (2003) 288.
[16] N.J.M. Carvalho, B.J. Kooi, J.Th.M. De Hosson, in: C.A. Brebbia, J.Th.M. deHosson, S.-I. Nishida (Eds.), Surface Treatment VI: Computer Methods and Experimental Measurements for Surface Treatment Effects, WIT Press, Southampton, 2002, p. 233.
[17] N.J.M. Carvalho, V. Sivel, J.Th.M. De Hosson, Acta Mater. (submitted for publication).
[18] N.J.M. Carvalho, J.Th.M. DeHosson, Surf. Eng. 17 (2) (2001) 105.
[19] W. Weibull, J. Appl. Mech. 18 (1951) 293.
[20] P.Eh. Hovsepian, Y.N. Kok, A.P. Ehiasarian, A. Erdemir, J.-G. Wen, I. Petrov, Thin Solid Films 447–448 (2004) 7.
[21] W.J. Meng, R.C. Tittsworth, L.E. Rehn, Thin Solid Films 377–378 (2000) 222.
[22] D. Galvan, Y.T. Pei, J.Th.M. De Hosson, A. Cavaleiro, Surf. Coat. Technol. 200 (1–4) (2005) 739.